



HAL
open science

Magnetic and structural properties of biogenic magnetic nanoparticles along their production process for use in magnetic hyperthermia

Claire Carvallo, Anaïs Fondet, Raphaël Le Fèvre, Dario Taverna, Yohan Guyodo, Imène Chebbi, Vincent Dupuis, France Lagroix, Malika Khelfallah, Jean-Michel Guigner, et al.

► To cite this version:

Claire Carvallo, Anaïs Fondet, Raphaël Le Fèvre, Dario Taverna, Yohan Guyodo, et al.. Magnetic and structural properties of biogenic magnetic nanoparticles along their production process for use in magnetic hyperthermia. *Journal of Magnetism and Magnetic Materials*, 2023, 575, pp.170726. 10.1016/j.jmmm.2023.170726 . hal-04093875

HAL Id: hal-04093875

<https://hal.science/hal-04093875v1>

Submitted on 10 May 2023

HAL is a multi-disciplinary open access archive for the deposit and dissemination of scientific research documents, whether they are published or not. The documents may come from teaching and research institutions in France or abroad, or from public or private research centers.

L'archive ouverte pluridisciplinaire **HAL**, est destinée au dépôt et à la diffusion de documents scientifiques de niveau recherche, publiés ou non, émanant des établissements d'enseignement et de recherche français ou étrangers, des laboratoires publics ou privés.

1 **Magnetic and structural properties of biogenic magnetic nanoparticles along their**
2 **production process for use in magnetic hyperthermia**

3

4 **C. Carvalho^{1*}, A. Fondet², R. Le Fèvre³, D. Taverna¹, Y. Guyodo⁴, I. Chebbi³, V.**
5 **Dupuis⁵, F. Lagroix⁴, M. Khelfallah¹, J.-M. Guigner¹, F. Guyot¹, E. Alphandéry^{1,3}, A.**
6 **Juhin¹**

7

8 ¹Sorbonne Université, MNHN, CNRS, UMR 7590, Institut de Minéralogie, de Physique des
9 Matériaux et de Cosmochimie, F-75005 Paris, France

10 ²CEMES-CNRS, Université de Toulouse, Université Toulouse III – Paul Sabatier (UPS),
11 Toulouse, France

12 ³Nanobacterie SARL, 36 Boulevard Flandrin, 75016, Paris, France

13 ⁴Université Paris Cité, Institut de Physique du Globe de Paris, CNRS, Paris, F-75005, France.

14 ⁵PHENIX Laboratoire, CNRS, Sorbonne Université, F-75005, Paris, France

15 *Corresponding author; email: Claire.carvallo@sorbonne-universite.fr

16 **Abstract**

17 Iron-oxide nanoparticles synthesized by magnetotactic bacteria can be used in cancer
18 treatment by means of magnetic hyperthermia. In order to study the structural properties of
19 samples through the successive steps of their production from cultivated magnetotactic
20 bacteria to coated magnetosomes, and their effect on magnetic properties, we performed a
21 combination of (cryo-)Transmission Electron Microscopy observations and magnetic
22 hysteresis as well as First-Order Reversal Curve diagrams at low temperature. The anisotropy
23 of magnetic interactions was investigated by recording field-cooled FORC diagrams with a
24 measuring field either parallel or perpendicular to the field-cooling direction. The results from
25 the various techniques are in very good agreement. We found that magnetosomes in
26 magnetotactic bacteria are arranged in chains and have magnetic properties typical of stable
27 single-domain aligned particles. Extracted magnetosomes form clusters of interacting
28 maghemite particles with some remaining chains, while purified magnetosomes are solely
29 arranged in clusters. Finally, magnetosomes coated with 1,2-dioleoyl-sn-glycero-3-
30 phosphocholine (DOPC) are still organized in clusters but with less magnetostatic interactions
31 than in purified magnetosomes, while magnetosomes coated with citric acid tend to recover a
32 chained structure forming loops. The main features observed on the FORC diagrams are
33 consistent with the various arrangement observed. Lastly, hyperthermia properties were
34 measured for the two coated samples and we found that magnetosomes coated with citric acid
35 display a higher Specific Absorption Rate and therefore hold a better potential for biomedical
36 applications.

37

38

39 **Index terms**

- 40 FORC diagram, Magnetic hyperthermia, Magnetosomes, Magnetotactic bacteria,
- 41 Transmission Electron Microscopy

42

1- Introduction

43 The production and use of iron oxide nanoparticles (IONPs) in cancer treatment has been
44 studied for the last twenty years with the goal of targeting tumors more accurately, thus
45 avoiding damage to healthy cells of patients [1]. Treatment of cancer with IONPs can be
46 achieved by magnetic hyperthermia by heating nanoparticles through the application of an
47 alternating magnetic field to eradicate a tumor through localized moderate heating. IONPs are
48 already commercialized for the treatment of iron deficiency anemia diseases [2] and several
49 types of cancers [1]. In terms of toxicity, IONPs are particularly attractive mostly because
50 liver and kidneys easily eliminate them after completion of injection and treatment [3].

51 Magnetosomes, which are synthesized by magnetotactic bacteria (MTB), appear to be at the
52 most advanced stage of development among the different types of bio-synthesized IONPs (see
53 [3] for a review). In nature, MTB use magnetosomes as a "magnetic compass" guiding them
54 in the direction of the Earth's magnetic field [4]. This capacity enables bacteria to orientate
55 and find mediums in water that are best adapted to their needs. Magnetosomes present several
56 interesting characteristics: particles have a homogeneous size distribution and uniform
57 morphology [5], they are composed of high crystallinity magnetite and/or maghemite [5], and
58 their magnetic moment is stable at room temperature [6]. Moreover, biocompatible iron oxide
59 magnetosomes are free of elements that are not compatible with medical treatment and
60 injection in the body [7], and they can be produced in large quantities by cultivation in non-
61 toxic growth medium [8]. The chain structure of the magnetosomes, which cannot be
62 controlled accurately when using chemically synthesized IONPs, results in unique structural
63 and magnetic properties of magnetosomes.

64 In this work, we characterize the magnetic and structural properties of MTB-derived
65 IONPs at various stages of their production, i.e., from whole bacteria (Sample 1), extracted
66 magnetosomes (Sample 2), purified magnetosomes (Sample 3), to coated magnetosomes with

67 two different coating agents (Samples 4 and 5), as potential candidates for hyperthermia. The
68 MTB used in this study are MSR-1 *Magnetospirillum gryphiswaldense* (referred to as MSR-
69 1). The coating for the last two samples is necessary to make the magnetosomes
70 biocompatible for cancer treatment [9, 10]. Magnetosomes extracted from MSR-1 have been
71 shown to be less toxic and more efficient than chemically synthesized nanoparticles coated
72 with amino-silane used in nanomedicine [11] and are bio-compatible [7, 12, 13]. Here, the
73 coating agents were chosen based on their different effects on the arrangement of
74 magnetosomes.

75 Transmission Electron Microscopy (TEM) and cryo-TEM observations were
76 conducted to determine the distribution of magnetosome sizes and the structural organization
77 of magnetosomes. Measurements of hysteresis curves and First-Order Reversal Curve
78 (FORC) diagrams were performed at low temperature to identify the magnetic domain state of
79 the magnetosomes, to provide insight into particle size distribution and spatial organization
80 [14], [15], and to determine coercivity and magnetic interaction distribution, for which FORC
81 diagrams are an ideal tool (see [16] for a review). Finally, measurements of the Specific
82 Absorption Rate (SAR) were performed for both coated magnetosome samples, in order to
83 assess their heating capacities under the application of an alternating magnetic field.

84 Because we carry out (cryo-)TEM observations and FORC diagram measurements
85 together, our study provides insight about the effect of magnetosome arrangement, which
86 depends on the sample type, on the distribution of magnetic properties measured with FORC
87 diagrams, in particular the marginal and vertical distributions. Finally, because FORC
88 diagrams were measured at low temperature, we can also assess the effect of field-
89 cooled/zero-field-cooled treatment on the FORC diagrams and obtain information about the
90 anisotropy of the two distributions derived from FORC diagrams. Such low-temperature
91 FORC measurements on samples in solution are seldom carried out.

92

93

2- Experimental method

94 2.1.1. Sample synthesis

95 Five samples were studied in the present work, all of them produced by the Nanobacterie
96 Company. They were collected at the five different steps of the typical production process for
97 cancer treatment applications of magnetosomes, each sample corresponding to a different
98 step. The five samples are as follows:

99 - Sample 1: MSR-1 bacteria, in their culture medium, at a concentration of 4.10^9
100 cells/mL.

101 - Sample 2: magnetosomes extracted from bacteria through lysis, by placing bacteria in
102 a basic medium composed of KOH and heating to 90 °C. Magnetosomes were
103 subsequently collected with a magnet and put in water. The concentration was 50 mg
104 of Fe/mL.

105 - Sample 3: purified magnetosomes, heated in air to 380 °C. Most biological material is
106 thus removed from the magnetosomes, though there could be some phosphate
107 residues. The concentration was also 50 mg of Fe/mL.

108 - Sample 4: magnetosomes coated with 1,2-dioleoyl-sn-glycero-3-phosphocholine
109 (DOPC), which is a bitailed phospholipid. It is a bio-compatible molecule and
110 therefore bio-applied. The concentration was 25 mg of Fe/mL.

111 - Sample 5: magnetosomes coated with and 2-Hydroxypropane-1,2,3-tricarboxylic acid
112 (citric acid, CA). The concentration was also 25 mg of Fe/mL.

113 Culture of MTB in 7.5L fermenter, extraction, and purification of magnetosomes were
114 performed as described in [17]. Iron concentrations were determined with a colorimetric
115 dosage with a 5% precision [18]. The coating for the last two samples is a necessary
116 condition, both to stabilize magnetosomes in water and to make them compatible with

117 injection in a patient's body for cancer treatment. Coating in citric acid (CA) favors the
118 formation of chains because it is a triacid that enables the complexation of Fe with several
119 magnetosomes, leading to a chain-like structure [18], [19]. On the contrary, 1,2-dioleoyl-sn-
120 glycerol-3-phosphocholine (DOPC) coating favors interactions between phosphate groups of
121 the coating and Fe oxide, leading to a nano-micelle type structure [20]. Moreover, the
122 proportion of DOPC at the surface of purified magnetosomes is not sufficient to induce
123 hydrophobicity in the nanoparticle suspension. Therefore, these coated magnetosomes are not
124 soluble but behave as a stable suspension. Sample 1 was stored at -80°C in a freezer while the
125 other four samples were stored at 4°C in a cold room.

126

127 *2.2. TEM and cryo-TEM observations*

128 TEM and cryo-TEM observations were carried out at IMPMC in order to characterize
129 magnetosomes and their organization within the different samples. Cryo-TEM in particular
130 allows preserving the integrity of bacteria as well as the organization of nanoparticles, since it
131 does not require drying the sample on a TEM grid. Standard TEM observations were realized
132 with a Jeol 2100F equipped with a Schotky FEG gun, and cryo-TEM observations with a Jeol
133 2100, equipped with a LaB6 gun.

134 For Sample 1 preparation observed with standard TEM, the sample was diluted 400 times, the
135 solution was centrifuged 10 min at 14500 rpm. The supernatant was removed, replaced by
136 deionized water, and centrifugation and change of supernatant was re-iterated a second time.
137 This was done to remove the culture medium which can alter the observation on the TEM-
138 grid once dried. 2.5 μL of the obtained solution was deposited on an ionized TEM grid, and
139 dried for 24 hours at room temperature. For Samples 2 and 3, diluted solutions at a concentra-
140 tion of 100 μg of Fe/mL were deposited on a TEM-grid and dried for 24 hours at room tem-
141 perature.

142 For cryo-TEM images, a 5 μL drop of the initial sample solution was deposited on
143 “Quantifoil”[®] (Quantifoil Micro Tools GmbH, Germany) carbon membrane grids. The ex-
144 cess of liquid on the grid was absorbed with a filter paper and the grid was quench-frozen
145 quickly in liquid ethane to form a thin vitreous ice film using an homemade mechanical cryo
146 plunger. Once placed in a Gatan 626 cryo-holder cooled with liquid nitrogen, the samples
147 were transferred in the microscope and observed at low temperature (-180 °C). Cryo-TEM
148 images were recorded on ultrascan 1000, 2k x 2k pixels CCD camera (Gatan, USA), using a
149 LaB₆ JEOL JEM2100 (JEOL, Japan) cryo microscope operating at 200kV with a JEOL low
150 dose system (Minimum Dose System, MDS, JEOL, Japan) to protect the thin ice film from
151 any irradiation before imaging and reduce the irradiation during the image capture.

152 *2.3. Magnetic measurements*

153 **Hysteresis loops-** Hysteresis loops were measured with a Physical Properties Measurement
154 System (PPMS) coupled with a Vibrating Sample Magnetometer (VSM) at the Low-
155 temperature Physical Measurements Platform of Sorbonne Université. Hysteresis loops were
156 measured from -3T to 3T. Samples 4 and 5 were measured in solution, Sample 3 as a powder
157 because of its tendency to sediment very quickly when dispersed in solution, and Sample 2
158 both in solution and as a powder. Sample 1 was not measured because its magnetization was
159 expected to be too weak. Temperature was varied between 5 and 300 K except for Samples 2
160 and 3 as powders that were measured both at 10 and 300 K. Samples were weighted and
161 magnetizations were normalized to mass.

162

163 **FORC diagrams** - FORC diagrams allow a qualitative characterization of the magnetic
164 domain structure and magnetostatic interactions, by measuring a set of partial hysteresis
165 curves that originate from the descending branch of the hysteresis loop [15], [21]. FORC
166 diagrams were measured with a magnetometer (μ -VSM) equipped with a cryostat from

167 Princeton Measurements Corporation at the IPGP-IMPMC Mineral Magnetism Analytical
168 Facility. For stable single domain (SSD) particles with weak interactions, the FORC
169 distribution along the vertical axis can be interpreted as the distribution of the particle
170 interaction fields, and the marginal FORC distribution, which corresponds to the total
171 magnetic contribution of all particles with a given switching field, as the coercivity
172 distribution of the system [22].

173 FORC diagrams were each calculated from 130 individual FORCs measured with a field step
174 of 2 mT, at a temperature of 50 K, and with an averaging time of 0.2 s. The measurement time
175 for each FORC diagram was about one hour. The temperature of 50 K was chosen in order for
176 the results to be comparable with results from cryo-TEM and hysteresis. They were
177 subsequently analysed with the Forcinel software [23], with a variable smoothing factor [24].
178 The variable smoothing considerably reduces the noise levels by applying larger smoothing
179 factors to the background, while preserving the areas along the axes with relatively small
180 smoothing factors.

181 For each of the five samples, three FORC diagrams were measured. First, solutions containing
182 20 μ L of each magnetosome sample was prepared and enclosed in a polycarbonate gelcap and
183 placed between the coils. The sample was cooled in zero-field to 50 K, and a first FORC
184 diagram was measured (ZFC measurement). Then, the sample was re-heated to room
185 temperature, and cooled in a field of 0.5 T back to 50 K. A second FORC diagram was
186 measured (FC measurement). Finally, the VSM head, to which the sample is attached, was
187 turned by 90° and a third FORC diagram was measured (FC90 measurement).

188

189 *2.4. Hyperthermia measurements*

190 Hyperthermia measurements are used to gain information about the heating power of a
191 sample, i.e. the ability of the sample to release heat when submitted to an alternating magnetic

192 field (AMF). It is an important measurement to evaluate the efficiency of a sample in
193 potential cancer treatment. Temperature is acquired as a function of time, during the
194 application of an AMF, until an equilibrium temperature is reached (about 15 min). The SAR
195 is then calculated using the slope of the curve T(t) at the origin, as:

$$SAR = \frac{c_{water}}{\chi_{Fe}} \times \frac{\Delta T}{\delta t}$$

196 with χ_{Fe} the iron concentration of the sample and c_{water} the heat capacity of water in J.L⁻¹.K⁻¹,
197 and SAR expressed in W/g.

198 The AMF was set at 31 mT with a frequency of 198 kHz. Hyperthermia was only measured
199 on the two coated samples (Samples 4 and 5) potentially used for cancer treatment, and for
200 three different concentrations of each sample (2.5, 5 and 10 mg(Fe)/mL) in order to track a
201 possible concentration dependence of SAR. The temperature measurements within the sample
202 were conducted in triplicates. The median and standard deviation for each point of the T(t)
203 curves was used to obtain minimum, median and maximum SAR values.

204

205

3- Results

206 *3.1. Structural organization of magnetosomes from TEM and cryo-TEM*

207 Samples 1, 4 and 5 were successfully observed with cryo-TEM, while Samples 2 and 3 were
208 observed with standard TEM, as extracted uncoated magnetosomes tend to aggregate too
209 rapidly during cryo-TEM grid preparation, and the resulting large clusters of particles are not
210 suitable to the scope of studying their self-organization by cryo-TEM. Sample 1 was also
211 observed with standard TEM.

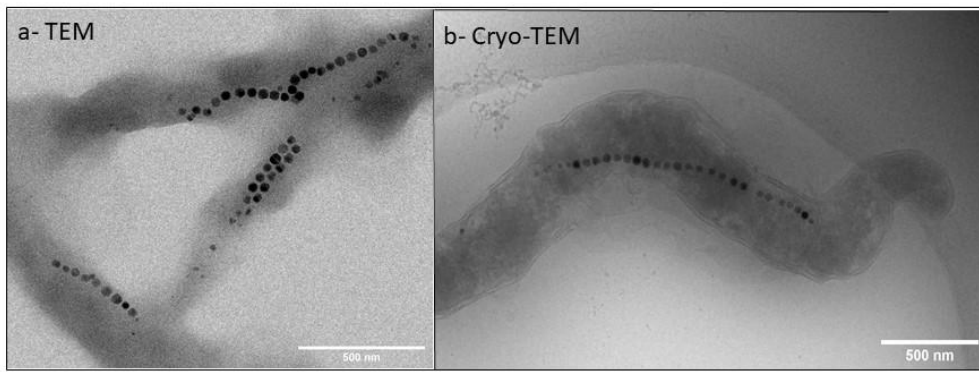
212 Chains of magnetosomes are clearly visible in Sample 1 under standard TEM (Fig. 1a) and
213 cryo-TEM (Fig. 1b). However, bacteria tend to aggregate more on standard TEM grids, and

214 their boundaries are difficult to identify with the image contrast. Double chains were
215 sometimes observed within individual bacteria. The length of chains ranges from 122 nm to
216 1.5 μm , with a mean length of 624 nm. They are composed on average of 14 magnetosomes
217 (Fig. A-1a, f, g). Magnetosome shapes vary from rounded to cubic and cuboctahedral.
218 Following a rounded shape approximation for all particles, magnetosomes have a mean
219 diameter of 34.6 nm, with a standard deviation of 6.9 nm. The interparticle distance is $11.2 \pm$
220 4.2 nm.

221 Sample 2 consists of extracted magnetosomes, arranged in chains and agglomerates of
222 particles (Fig. 2a, b). Chains are attached to clusters of particles, at least at one end. The
223 length of chains ranges from 200 nm to 1.6 μm , with an average length of 678 nm, and are
224 composed of 18.4 magnetosomes on average (Fig. A-1b, h). Individual magnetosomes have a
225 mean diameter of 35.1 nm (standard deviation of 5.6 nm).

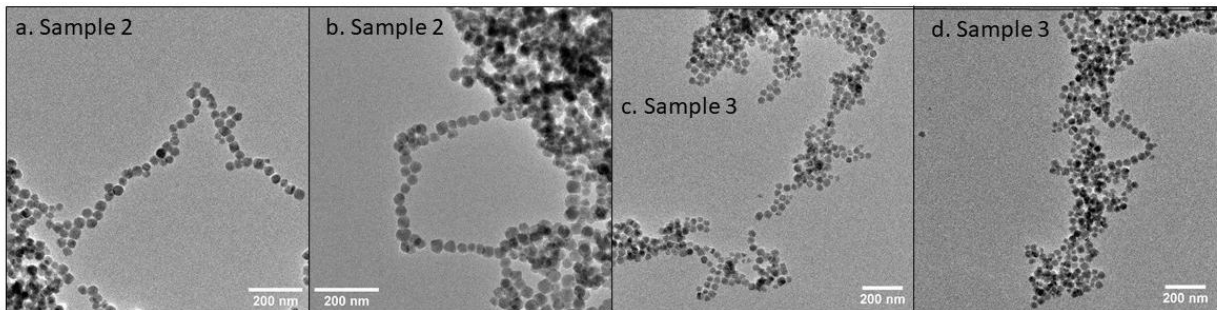
226 Sample 3 is composed of purified magnetosomes, i.e. magnetosomes removed from their
227 original organic membrane. Magnetosomes in this sample have a mean particle size of 35.1
228 nm (standard deviation of 5.4 nm). This particle size is similar to that in Sample 2, although
229 there are more particles in the 34-38 nm range in Sample 3 than in Sample 2 (60% vs. 55%)
230 (Fig. A-1c). TEM images show that particles are more likely to form agglomerates (Fig. 2c,
231 d), which was expected since magnetic interactions are now dominant and cause the
232 magnetosomes to be mechanically unstable in solution. We also observe less particles with a
233 diameter <20 nm in Samples 2 and 3 than in Sample 1: these particles represent 7.8% of
234 particles in Sample 1, but only 4 % in Sample 2 and 3.9 % in Sample 3.

235



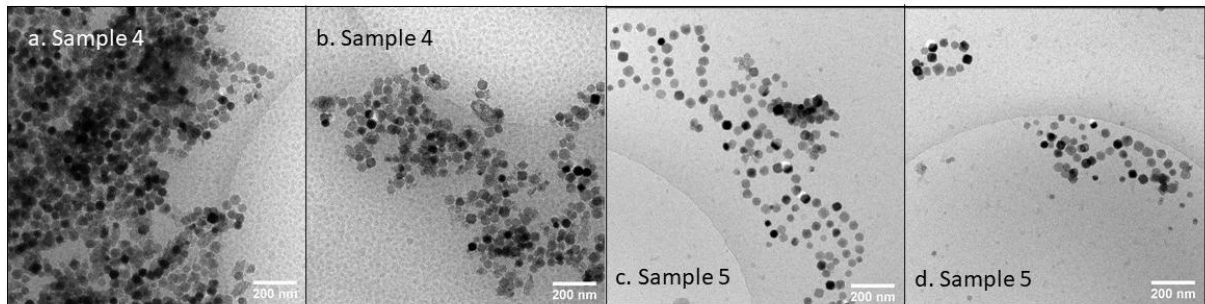
236

237 **Fig. 1:** TEM (panel a) and cryo-TEM (panel b) images of Sample 1.



238

239 **Fig. 2:** TEM images of Sample 2 (panels a, b) and Sample 3 (panels c, d).



240

241 **Fig. 3:** cryo-TEM images of Sample 4 (panels a, b) and Sample 5 (panels c, d).

242

243 Cryo-TEM observations of coated magnetosomes (Samples 4 and 5) show important
 244 differences depending on the coating agent. The magnetosomes of sample 4 are coated with
 245 DOPC and form aggregates (Fig. 3a, b), while magnetosomes of Sample 5 are coated with CA
 246 and tend to form organized rings with increased interparticle distances in comparison to other

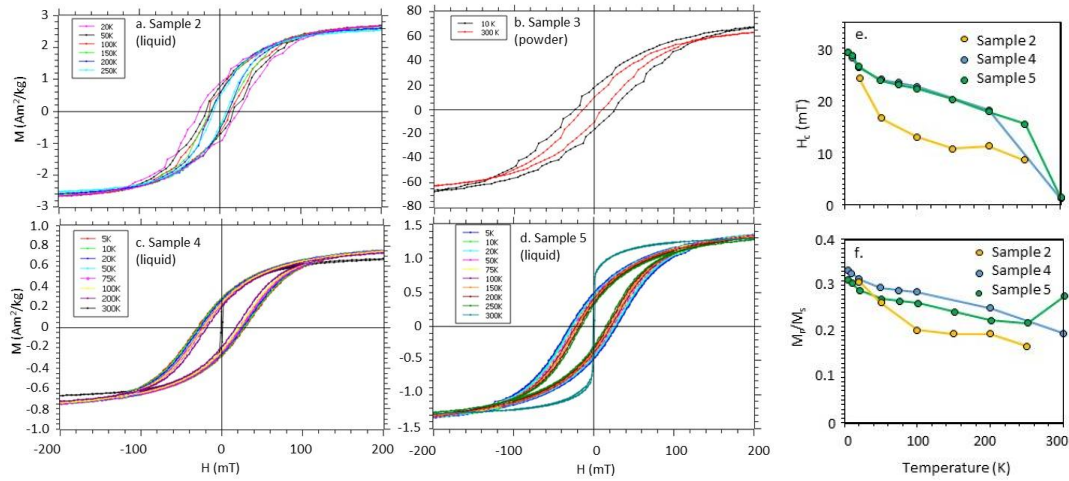
247 samples (Fig. 3c, d). The mean diameter of magnetosomes is similar for both coated samples:
248 40.9 nm (standard deviation of 8.1 nm) for Sample 4 and 41.5 nm (standard deviation of 7.3
249 nm) for Sample 5 (Fig. A-1d, e). The interparticle distance is 13.4 ± 4.3 nm for Sample 5.

250

251 *3.2. Magnetic hysteresis curves*

252 Hysteresis loops (Fig. 4a-d) show that, regardless of temperature, magnetization is saturated
253 in an applied magnetic field of 2 T for all samples. Hysteresis loops for Samples 4 and 5 close
254 progressively when temperature is increased from 5 to 250 K, and close more sharply above
255 250 K to room temperature. For Sample 2 (Fig. 4a), blocking seems to begin at lower
256 temperatures than for Samples 4 and 5. The variation of bulk coercivity (H_c) and the ratio of
257 remanent magnetization over saturation magnetization (M_r/M_s) reflect this behavior (Fig. 4
258 e,f): when temperature is increased, both H_c and M_r/M_s decrease. H_c then drops sharply at
259 room temperature (when measured). There is no evidence of a drop around 120 K, therefore
260 no evidence of a Verwey transition in any of the samples. The presence of maghemite rather
261 than magnetite is further confirmed by the value of saturation magnetization of Sample 2 (as a
262 powder, Fig. SI-2) measured as $75.87 \text{ Am}^2/\text{kg}$ at room temperature; a value that is close to the
263 known value of maghemite ($74.3 \text{ Am}^2/\text{kg}$ [25]). Moreover, heating curves of field-cooled and
264 zero-field cooled Saturation Isothermal Remanant Magnetization (SIRM) acquired at 10 K in
265 a 2.5T field on samples prepared identically to Samples 2 and 3 show that the Verwey
266 transition is not visible in heated extracted magnetosomes as well as in purified
267 magnetosomes [26] (Fig. A-3).

268



269

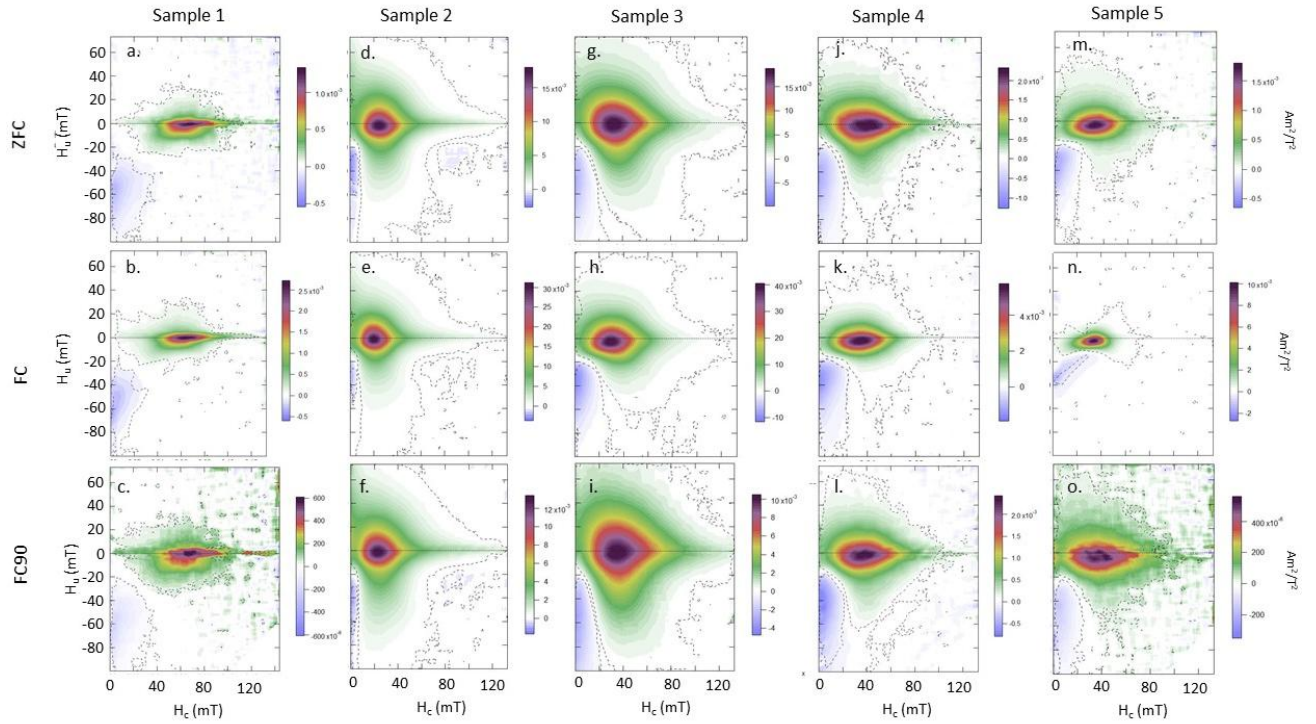
270 **Fig. 4:** Magnetization curves measured for Samples 2 (panel a), 3 (panel b), 4 (panel c) and 5
 271 (panel d). All samples except Sample 3 are in solution. Variation of hysteresis ratio M_r/M_s
 272 (panel d) and coercivity H_c (panel e) as function of temperature, derived from the
 273 corresponding hysteresis loops.

274

275 3.3. Distribution of magnetic properties from FORC diagrams

276 The FORC diagrams measured for the five samples in the three different configurations (ZFC,
 277 FC and FC90 (see caption of Fig. 5 for the meaning of acronyms)) are shown in Fig. 5. They
 278 are all plotted on the same (H_c , H_u) scale and with the same smoothing parameters.

279



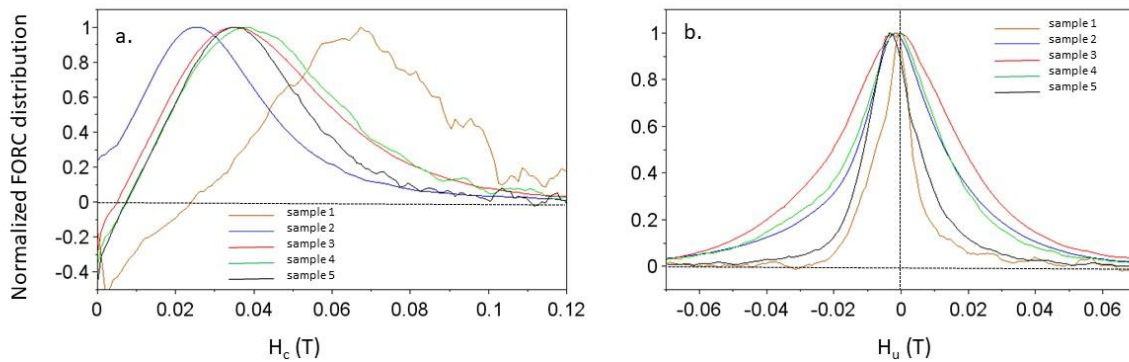
280

281 **Fig. 5:** FORC diagrams measured for Sample 1 (a, b, c), Sample 2 (d, e, f), Sample 3 (g, h, i);
 282 Sample 4 (j, k, l), Sample 5 (m, n, o). Panels (a, d, g, j, m) correspond to zero-field cooled
 283 (ZFC) measurements, panels (b, e, h, k, n) to field-cooled (FC) measurements, and panels (c,
 284 f, i, l, o) to measurements after FC and turning the sample by 90° (FC90).

285

286 In the ZFC configuration (i.e., the usual configuration when measuring FORC diagrams), the
 287 FORC diagram measured for Sample 1 (Fig. 5a) is typical of MTB (e.g., [27]). The extended
 288 coercivity distribution between 40 and 100 mT and the very narrow contours along the
 289 vertical axis are expected for weakly interacting single domain magnetite particles. Samples 2
 290 and 3 (Fig. 5d, g) show FORC diagrams with a “teardrop” shape typical of strongly
 291 interacting systems (e.g., [22], [28]). This shape is still visible on the FORC diagram of
 292 Sample 4 (Fig. 5j), while contours for Sample 5 have a more elliptical shape intermediate
 293 between those of Sample 1 and Sample 2 (Fig. 5m). These differences in coercivity
 294 distribution are reflected on the marginal distribution (Fig. 6a): Sample 1 has the largest

295 coercivity distribution that is also centered on the highest coercivity value, while the
 296 coercivity distribution for Sample 2 is shifted towards lower values. The vertical profile
 297 across the maximum of the FORC distribution (Fig. 6b), which is often used as a rough
 298 estimate of the amount of magnetic interactions, is widest for Samples 3, and narrower for
 299 Samples 1 and 5.



300
 301 **Fig. 6:** a. Marginal coercivity distribution for the five samples in ZFC configuration. b.
 302 Vertical FORC profile through the maximum of the FORC distribution for the five samples in
 303 ZFC configuration.

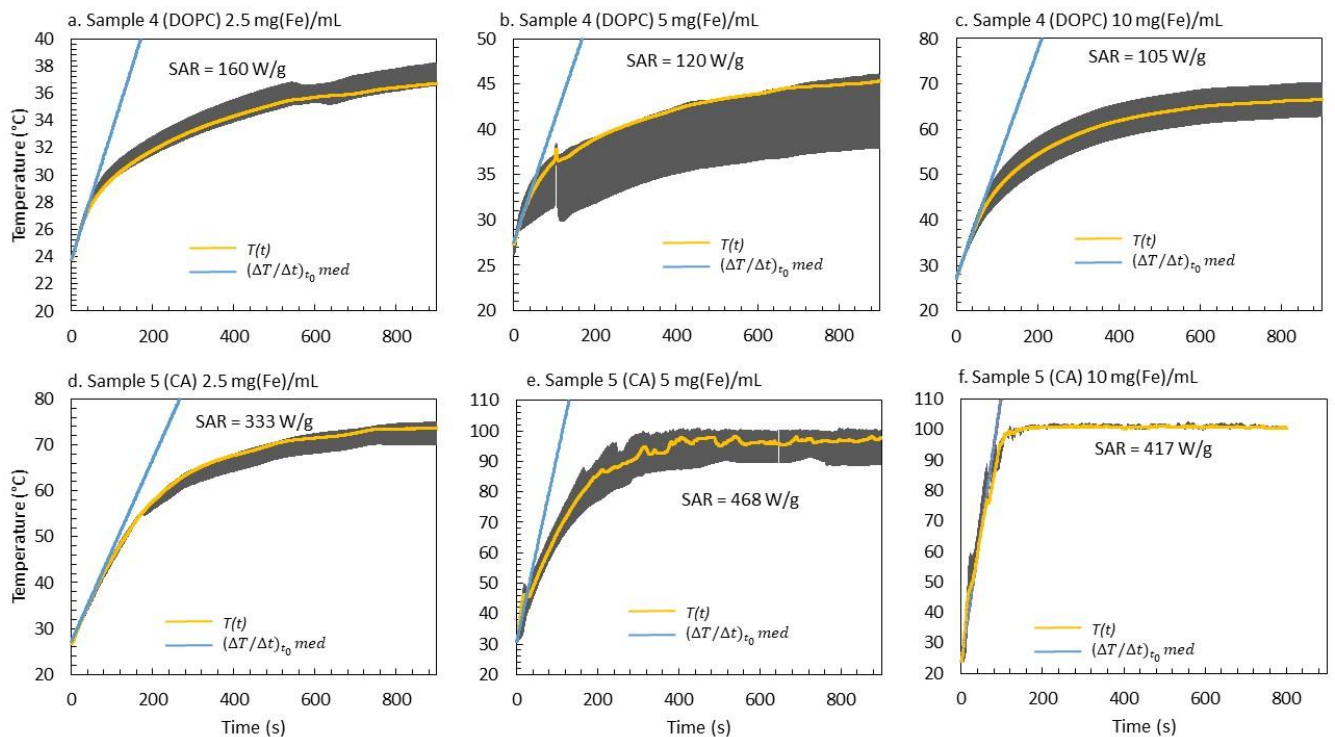
304 The FC FORC diagrams show a similar evolution to the ZFC ones when comparing the five
 305 samples. However, the contours are less spread out than for the ZFC FORC diagrams, both
 306 along the vertical and horizontal directions. The lobe observed in the lower half of the ZFC
 307 diagram for Samples 2, 3 and 4 is faint (Samples 2 and 3) or inexistent (Sample 4) in the
 308 corresponding FC diagram. Finally, the shapes of the FC90 FORC diagrams are rather similar
 309 to that of the ZFC FORC diagrams. The only notable difference is the higher noise level
 310 caused by the lower values taken by the FORC distribution themselves.

311
 312 *3.4. Hyperthermia measurements*

313 Hyperthermia measurements were carried out on three different concentrations of Samples 4
 314 and 5. The heating temperature after 850 s, for both samples, increases with sample

315 concentration (Fig. 7). For each of the three concentrations, the heating temperature is higher
 316 for Sample 5 (coated with CA) than for Sample 4 (coated with DOPC). Sample 5 reaches a
 317 temperature of 74°C for a concentration of 2.5 mg(Fe)/mL, 97°C for 5 mg(Fe)/mL and 100°C
 318 for 10 mg(Fe)/mL. Sample 4 reaches only 36.4°C for a concentration of 2.5 mg(Fe)/mL, 47.5
 319 °C for 5 mg(Fe)/mL and 66.5°C for 10 mg(Fe)/mL. Consistently, the calculated SAR values
 320 are higher for Sample 5 than for Sample 4, regardless of sample concentration. For Sample 4,
 321 the SAR decreases with increasing concentration, while no similar trend is observed for
 322 Sample 5, even though the SAR values differ for the different concentrations.

323



324

325 **Fig. 7:** Hyperthermia measurements of temperature (T) as a function of time (t) for Sample 4
 326 (panels a, b, c) and Sample 5 (panels d, e, f) for various sample concentrations: a, d: 2.5
 327 mg(Fe)/mL; b, e : 5 mg(Fe)/mL ; c, f : 10 mg(Fe)/mL. The alternating magnetic field (AMF)
 328 intensity is 31 mT and its frequency is 198 kHz. The yellow lines show the mean values T(t);
 329 the grey area represents the error bar on T. The SAR value indicated on each figure panel is
 330 calculated as the average of maximum, minimum and median values.

331
332

4- Discussion

333 The various observations and measurements presented in this study allow to finely
334 characterize the structural and magnetic properties of magnetosomes through the whole
335 process of transformation from MSR-1 raw MTB to coated magnetosomes that could be
336 potentially used for cancer treatment. Because FORC diagrams strongly depend on the
337 arrangement of individual particles in a sample, we can also observe the effects of these
338 structural properties on the FORC features. However, it should be kept in mind that samples
339 observed in cryo-TEM are prepared in a substrate in 2D configuration while for magnetic
340 measurements the sample is prepared in a 3D configuration.

341

342 *4.1. Comparison of structural and magnetic properties between samples*

343 The structural particle organization determined from (cryo-)TEM images agrees well with the
344 evolution of magnetic properties measured in FORC diagrams. Magnetosomes in Sample 1
345 are organized in chains, each chain being (in most images) isolated in a bacteria cell. This is
346 consistent with the small amount of interactions inferred from the narrow FORC vertical
347 profile (Fig. 6b). The strong shape anisotropy due to the chain organization is responsible for
348 the high coercivities observed on the marginal coercivity distribution (Fig. 6a).

349 In Sample 2, magnetosomes aggregate in clusters (Fig. 2a, b), which is reflected in the FORC
350 distribution that widens in the vertical direction due to increased magnetic interactions
351 between magnetosomes. The whole coercivity distribution is shifted towards lower
352 coercivities as a result of the partial collapse of the chains. This trend continues for Sample 3
353 for which clusters are even denser and magnetic interactions are stronger than for Sample 2.

354 Both coated samples (Samples 4 and 5) show less magnetic interactions than extracted
355 (Sample 2) and purified (Sample 3) magnetosomes. Indeed, Sample 5 is characterized by a
356 narrow vertical FORC profile, which is consistent with the ring arrangement of

357 magnetosomes that was observed with cryo-TEM (Fig. 3 c,d). However, for Sample 4 (coated
358 with DOPC) TEM images show highly clustered magnetosomes for which we would expect
359 strong magnetic interactions, which is not consistent with the small amount of spreading of
360 the FORC diagram along the vertical axis. A possible interpretation is that the DOPC coating
361 may help reduce interactions even though magnetosomes are clustered. This result could also
362 be explained by the relative instability of the DOPC coating with time at room temperature:
363 although we expected DOPC coated samples to arrange in chains, we did not observe such an
364 organization on cryo-TEM images, which seems to indicate that the coating and thus the
365 organization of magnetosomes has been altered when exposed to room temperature. Citric
366 acid appears to be a more stable coating, which prevents particles to agglomerate. Moreover,
367 we envision that the organization of CA-coated magnetosomes may depend on the thickness
368 of coating, which would deserve more investigation in a future work.

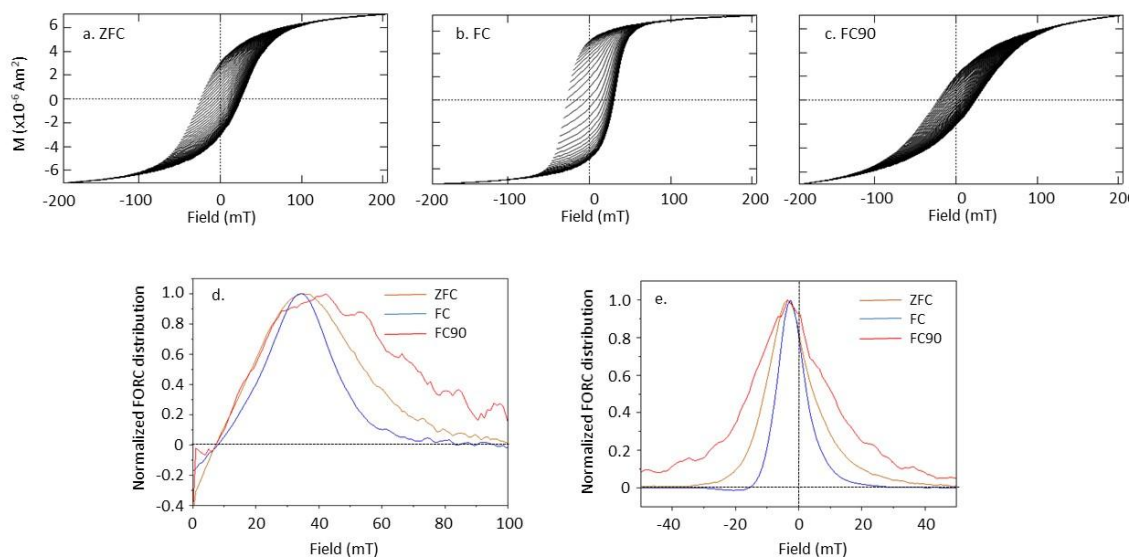
369

370 *4.2. Anisotropy of magnetic interactions*

371 For samples in solution, measurements of informative FORC diagrams can only be performed
372 at temperatures below the freezing point of water. However, it is possible to orientate the
373 magnetic moments of particles by applying a magnetic field before the sample is frozen. By
374 comparing FORC diagrams measured after field cooling, either with a magnetic field kept in
375 the same initial direction (FC) or in a perpendicular direction to the initial (FC90), the
376 anisotropy of magnetic interactions, which is connected to the anisotropy of particle
377 organization, can be further investigated.

378 Because magnetosomes tend to form linear chains when a magnetic field is applied, their
379 collective behavior is similar to that of a collection of elongated particles for which shape
380 anisotropy dominates. In the FC configuration, all chains are oriented in the direction of the
381 field applied during the FORC measurement. The field is therefore applied along the easy

382 magnetization axis. As a consequence, during FORC measurement, individual magnetic
 383 moments tend to switch direction for a field range that is narrower than in the ZFC
 384 configuration (Fig. 8a, b) resulting in hysteresis and partial hysteresis curves to have a more
 385 squared shape and causing FORC diagram contours to be less extended both vertically and
 386 horizontally. By contrast, the FC90 configuration is equivalent to a measurement along the
 387 hard magnetization axis leading to magnetic moments switching over a large range of fields
 388 (Fig. 8c). Thus, hysteresis and partial hysteresis loops are more irreversible, and the FORC
 389 diagrams cover a larger surface. The ZFC FORC diagrams have shapes intermediate between
 390 the FC and the FC90 shapes. These results are fully consistent with the FORC diagrams
 391 measured in ZFC, FC and FC90 configurations by [29] on oriented chains of hexagonal cobalt
 392 nanoplates for which the easy axis was also aligned with the chain direction.



393
 394 **Figure 8:** FORCs measured on Sample 5. a: ZFC; b: FC; c: FC90 configurations. d: Marginal
 395 coercivity distributions. e: vertical profiles through the maximum of the FORC distribution
 396 for the corresponding FORC diagrams.

397
 398 These results can be further quantified by comparing the Full Width at Half Maximum
 399 (FWHM) of the marginal distribution (Fig. 8d, and Table 1). The marginal distribution

400 FWHM of the five samples is lowest in the FC configuration and highest in the FC90
401 configuration. The same trend is found for the FWHM of the vertical distribution (Fig. 8e, and
402 Table 1), except for Sample 4, for which the ZFC FWHM is slightly higher than the FC90
403 FWHM. The difference in FWHM values is more striking for samples forming chains, i.e.,
404 Samples 1, 2 and 5. This could be used as a mean of quantifying the amount of chains
405 compared to the amount of individual particles, though further work would be needed to
406 investigate this effect.

407

408 **Table 1:** Values of H_c (horizontal) and H_u (vertical) fields for which the FORC distribution is
409 maximum; Full Width at Half Maximum (FWHM) of the marginal coercivity distributions
410 and the vertical field distributions, for all the measured FORC diagrams.

Sample	FC/ZFC/FC90	H_c max (T)	H_u max (T)	FWHM marginal (T)	FWHM vertical (T)
1	ZFC	0.067	0.000	0.045	0.011
	FC	0.060	0.000	0.040	0.008
	FC90	0.064	-0.001	0.056	0.016
2	ZFC	0.025	-0.001	0.036	0.026
	FC	0.020	-0.001	0.030	0.023
	FC90	0.024	-0.001	0.039	0.031
3	ZFC	0.035	0.000	0.045	0.039
	FC	0.032	-0.002	0.038	0.024
	FC90	0.032	-0.001	0.052	0.052
4	ZFC	0.038	0.000	0.047	0.029
	FC	0.036	-0.001	0.037	0.017
	FC90	0.040	-0.002	0.047	0.024
5	ZFC	0.035	-0.004	0.036	0.017
	FC	0.034	-0.002	0.023	0.009
	FC90	0.042	-0.002	0.052	0.024

411

412 *4.3.Application to cancer treatment*

413 According to hyperthermia measurements, Sample 5 (coated with CA) presents better
414 hyperthermia properties than Sample 4 (coated with DOPC). The SAR and the heating
415 temperature are higher for Sample 5 than for Sample 4. As shown by TEM observations,

416 magnetosomes are arranged in chains forming rings in Sample 5, while there is no such
417 organization in Sample 4. FORC diagrams, and especially the vertical FORC profiles indicate
418 that magnetostatic interactions are weaker in Sample 5 than in Sample 4, which is expected
419 based on the chain (Sample 5) versus cluster (Sample 4) configuration. This is consistent with
420 the results of [30] and [31], in which the chain structure is shown to increase the SAR. This is
421 also consistent with the fact that CA is a triacid, which allows the complexation of Fe with
422 several magnetosomes, and therefore the re-formation of a chain-like structure [13].
423 Our SAR values can also be compared with the SAR value of 217 W/g measured in a
424 previous study on extracted magnetosomes produced in similar conditions as Sample 2 and
425 measured with parameters identical to those used in this study (Le Fèvre, unpublished data).
426 This value is intermediate between the SAR of the mostly unchained DOPC-coated
427 magnetosomes and that of the partially chained CA-coated magnetosomes. As magnetosomes
428 in Sample 2 are partially organized in chains, this is also consistent with the increase of SAR
429 with chain structure.

430

431

5- Conclusion

432 The evolution of structural properties of magnetosomes across the production steps are
433 consistent with the evolution of their magnetic properties and can be summarized as below:

- 434 1 Magnetosomes in MSR-1 bacteria are arranged in chains. The magnetic properties are
435 typical of stable single domain particles forming chains;
- 436 2 After extraction, magnetosomes tend to form clusters, but some chains remain.
437 Extracted and heated magnetosomes are composed of maghemite. The coercivity
438 decreases, and magnetostatic interactions increase.

439 3 After purification, magnetosomes form clusters of particles, and it is more difficult to
440 identify chains. Magnetostatic interactions increase with respect to extracted
441 magnetosomes.

442 4 Magnetosomes coated with DOPC remain organized in clusters. This coating is not
443 stable with respect to time and temperature. Magnetostatic interactions are comparable
444 to those of extracted magnetosomes.

445 5 Magnetosomes coated with CA tend to form chains arranged in rings. The ability of
446 particles to organize in larger structures has been recovered in this sample and
447 magnetic properties show similarities with those observed in bacteria. The CA-coated
448 sample displays enhanced hyperthermia properties compared to the DOPC-coated
449 magnetosomes and therefore is more interesting for biomedical applications.

450 Lastly, differences in FORC diagrams acquired after zero-field cooling, field cooling co-
451 axially to the measuring field and perpendicularly to the measuring field can be interpreted as
452 partly resulting from the configuration of magnetosomes, whether chains are formed or not.
453 Therefore, such measurements have the potential to help quantify the ability of magnetic
454 particles to form chains, a critical characteristic in biological applications.

455

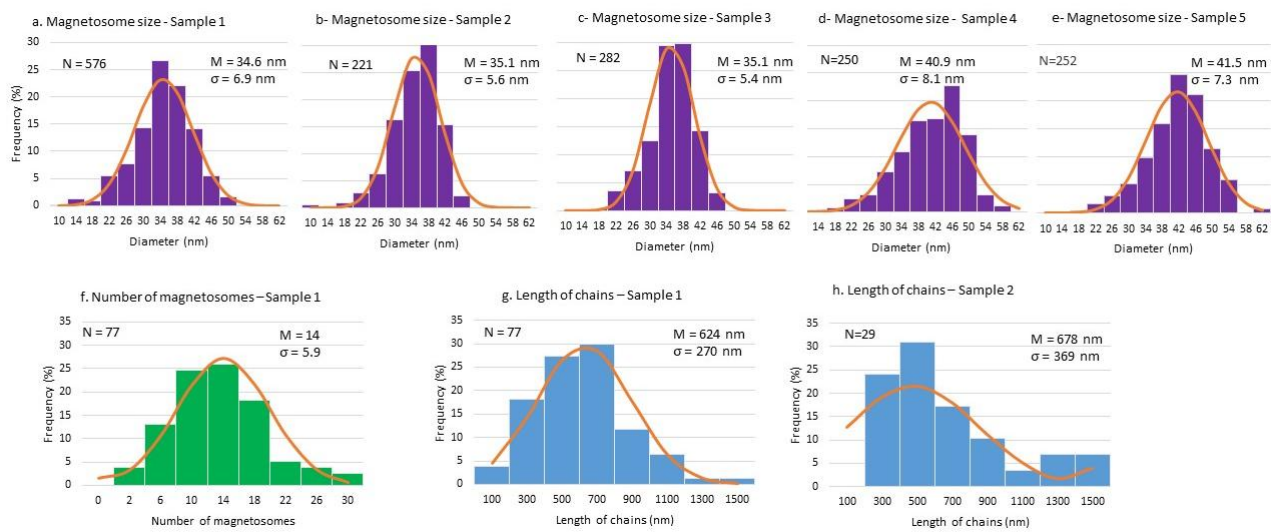
456 *Acknowledgements*

457 Authors acknowledge financial support from the French ANR under grant agreement 17-

458 CE30-0010-01.

459

460 **Appendix**

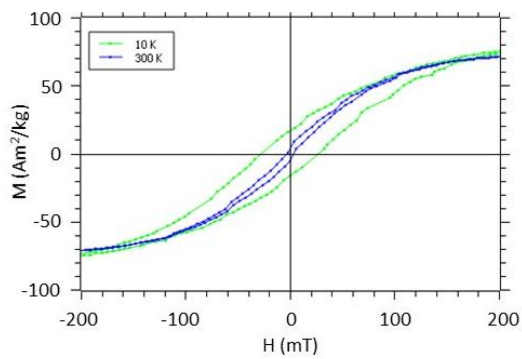


461

462 **Figure A-1:** Magnetosome size distributions for: a: Sample 1; b: Sample 2; c: Sample 3; d:

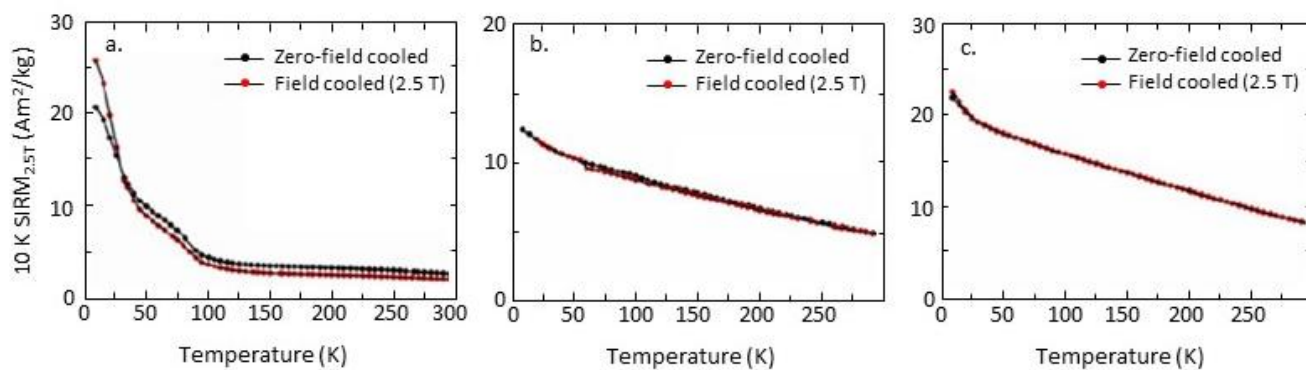
463 Sample 4; e: Sample 5; f: Distribution of the number of magnetosomes per chain for Sample

464 1; Length of chains distribution for: g: Sample 1; h: Sample 2.



465

466 **Figure A-2:** Magnetization curves measured for Samples 2 as a powder at 10 K (green curve)
467 and at 300 K (blue curve).



468
469 **Figure A-3:** Heating curve of SIRM acquired at 10 K in a 2.5 T field (Le Fèvre, unpublished
470 data). a: Extracted magnetosomes; b: Extracted magnetosomes heated for 2 hours at 200°C; c:
471 Purified magnetosomes (without membrane).

472

473

474 **References**

- 475 [1] Alphan ery, E., Iron oxide nanoparticles for therapeutic applications, *Drug Discovery*
476 *Today* 25 (2020) 141–149.
- 477 [2] Berny, C., Le F evre, R., Guyot, F., Blondeau, K., Guizonne, C., Rousseau, E., Bayan, N.,
478 Alphan ery, E., A method for producing highly pure magnetosomes in large quantity for
479 medical applications using magnetospirillum gryphiswaldense msr-1 magnetotactic bacteria
480 amplified in minimal growth media, *Frontiers in Bioengineering and Biotechnology* 8 (2020)
481 1–13.
- 482 [3] Alphan ery, E., Applications of magnetosomes synthesized by magnetotactic bacteria in
483 medicine, *Front. Bioeng. Biotechnol* (2014) doi: 10.3389/fbioe.2014.00005
- 484 [4] Blakemore, R., Magnetotactic bacteria, *Science* (1975) doi: 10.1126/science.170679
- 485 [5] Bazylinski, D.A., Frankel, R., Magnetosome formation in prokaryotes, *Nat. Rev.*
486 *Microbiol* (2014) doi:10.1038/nrmicro842
- 487 [6] Pan, Y., Peterson, N., Winklhofer, M., Davila, A.F., Liu, Q., Frederichs, T., et al., Rock
488 magnetic properties of uncultured magnetotactic bacteria, *Earth Planet. Sci. Lett.* (2005)
489 doi:10.1016/j.epsl.2005.06.029.
- 490 [7] Sun, J., Tang, T., Duan, J., Xu, P.X., Wang, Z., Zhang, Y., et al., Biocompatibility of
491 bacterial magnetosomes: acute toxicity, immunotoxicity and cytotoxicity, *Nanotoxicology*
492 (2010) doi:10.3109/17435391003690531
- 493 [8] Matsunaga, T., Tadokora, F., Nakamura, N., Mass culture of magnetic bacteria and their
494 application to flow type immunoassays, *IEEE Trans. Magn.* (1990) doi:10.1109/20.104444.

- 495 [9] Liu, G, Gao, J., Ai, H, Chen, X., Applications and potential toxicity of magnetic iron oxide
496 nanoparticles, *Small* (2013) doi: 10.1002/sml.201201531.
- 497 [10] Malhotra, N., Lee, J. S., Liman, R. A. D., Ruallo, J. M. S., Villaflores, O. B., Ger, T. R.,
498 Hsiao, C. D., Potential toxicity of iron oxide magnetic nanoparticles: a review, *Molecules*
499 (2020), doi: 10.3390/molecules25143159.
- 500 [11] Liu, R., Liu, J., Tong, J., Tang, T., Kong, W. C., Wang, X. W., Li, Y., Tang, J. T., Heating
501 effect and biocompatibility of bacterial magnetosomes as potential materials used in magnetic
502 fluid hyperthermia, *Progress in Natural Science: Materials International* (2012) doi:
503 10.1016/j/pnsc.2011.12.006
- 504 [12] Qi, L., Lv, X., Zhang, T., Jia, P., Yan, R., Zou, R., Yue, Y., Dai, L., Cytotoxicity and
505 genotoxicity of bacterial magnetosomes against human retinal pigment epithelium cells,
506 *Scientific Reports* (2016) doi: 10.1038/srep26961
- 507 [13] Nan, X., Teng, Y., Tian, J., Hu, Z., Fang, Q., A comprehensive assessment of the
508 biocompatibility of *Magnetospirillum gryphiswaldense* MSR-1 bacterial magnetosomes in
509 vitro and in vivo, *Toxicology* (2021) doi: 10.1016/j.tox.2021.152949
- 510 [14] Day, R., Fuller, M., Schmidt, V.A., Hysteresis Properties of Titanomagnetites: Grain-
511 Size and Compositional Dependence, *Physics of the Earth and Planetary Interiors* (1977) 13:
512 260-267.
- 513 [15] Roberts, A.P., Pike, C.R., Verosub, K.L., First- order reversal curve diagrams: A new
514 tool for characterizing the magnetic properties of natural samples, *Journal of Geophysical*
515 *Research: Solid Earth* (2000) doi: 10.1029/2000JB900326.
- 516 [16] Roberts, A. P., Heslop, D., Zhao, X., Pike, C. R. Understanding fine magnetic particle

517 systems through use of first-order reversal curve diagrams, *Reviews of Geophysics*, 557–602,
518 (2014) doi.org/10.1002/2014RG000462.

519 [17] Ngoc Nguyen, T, Chebbi, I., Le Fèvre, R., Guyot, F., Alphanféry, E., Non-pyrogenic
520 highly pure magnetosomes for efficient hyperthermia treatment of prostate cancer, *Applied*
521 *Microbiology and Biotechnology* (2023) 10.1007/s00253-022-12247-9

522 [18] Mandawala, C., Chebbi, I., Durand-Dubief, M., Le Fèvre, R., Hamdous, Y., Guyot, F.,
523 Alphanféry, E., Biocompatible and stable magnetosome minerals coated with poly-l-lysine,
524 citric acid, oleic acid, and carboxy-methyl-dextran for application in the magnetic
525 hyperthermia treatment of tumors, *Journal of Material Chemistry B*. (2017)
526 doi :10.1039/C6TB03248F

527 [19] E. Alphanféry and M. Durand-Dubief, “Apyrogenic preparation containing
528 nanoparticles synthesized by magnetotactic bacteria for medical or cosmetic applications”,
529 Patent No. CA2985163A1, 2020.

530 [20] H. Groult, J. Ruiz-Cabello, A. V. Lechuga-Vieco, J. Mateo, M. Benito, I. Bilbao, M. P.
531 Martinez-Alcazar, J. A. Lopez, J. Vasquez, and F. F. Herranz, “Phosphatidylcholine-Coated
532 Iron Oxide Nanomicelles for In Vivo Prolonged Circulation Time with an Antibiofouling
533 Protein Corona”, *Chemistry Europe*, vol. , pp. ,2014.

534 [21] Pike, C. R., Roberts, A.P., Verosub, K.L., Characterizing interactions in fine magnetic
535 particle systems using first order reversal curves, *J. Appl. Phys* (1999) 85: 6660-6667.

536 [22] Egli, R., Theoretical aspects of dipolar interactions and their appearance in first-order
537 reversal curves of thermally activated single-domain particles, *J. Geophys. Res.* (2006) doi :
538 10.1029/2006JB004567

- 539 [23] Harrison, R.J., Feinberg, J.M., FORCinel: An improved algorithm for calculating
540 first- order reversal curve distributions using locally weighted regression smoothing,
541 *Geochemistry, Geophysics, Geosystems* (2008) doi : 10.1029/2008GC001987.
- 542 [24] Egli, R., VARIFORC: An optimized protocol for calculating non-regular first-order
543 reversal curve (FORC) diagrams, *Global and Planetary Change* (2013) doi:
544 10.1016/j.gloplacha.2013.08.003.
- 545 [25] Dunlop, D., Özdemir, Ö., *Rock Magnetism, Fundamental and Frontiers*, Cambridge
546 *Studies in Magnetism*, Cambridge (1997).
- 547 [26] Lagroix, F., Le Fèvre, R., Alphanbéry, E., The below 50K quadrature magnetic
548 susceptibility anomaly in magnetite : what can we learn from magnetotactic bacteria? EOS
549 *Transactions of the AGU, Fall Meeting Supplement* (2018) Abstract GP43D-0796.
- 550 [27] Egli, R., Chen, A.P., Winkelhofer, M., Kodama, K.P., Horng, C.S., Detection of
551 noninteracting single domain particles using first-order reversal curve diagrams, *Geochem.*
552 *Geophys. Geosyst* (2010) doi : 10.1029/2009GC002916.
- 553 [28] Evans, M.E., Krasa, D., Williams, W., Winkelhofer, M., Magnetostatic interactions in a
554 natural magnetite-ulvöspinel system, *J. Geophys. Res* (2006) doi:10.1029/2006JB004454.
- 555 [29] Vargas, E., Denardin, J.C., Lavin, R., Mascaro, P., Chaneac, C., Coradin, P.,
556 Magnetization analysis of oriented chains of hexagonal cobalt nanoplates, *J. Appl. Phys.*
557 (2014) doi : 10.1063/1.4867345
- 558 [30] Alphanbéry, E., Faure, S., Seksek, O., Guyot, F., Chebbi, I., Chains of magnetosomes
559 extracted from AMB-1 magnetotactic bacteria for application in alternative magnetic field
560 cancer therapy, *ACS Nano* (2013) 5, 8: 6279-6296.

561 [31] Martinez-Boubeta, C., Simeonidis, K., Makridis, A., Angelakeris, M., Iglesias, O.,
562 Guardia, P., Cabot, A., Yedra, L., Estradé, S., Peiro, F., Saghi, Z., Midgley, P.A., Conde-
563 Leboran, I., Serantes, D., Baldomir, D., Learning from nature to improve the heat generation
564 of iron-oxide nanoparticles for magnetic hyperthermia applications, *Sci. Rep.* (2013)
565 doi:10.1038/srep01652.

566